Journal of
Materials Chemistry A

PAPER

Cite this: J. Mater. Chem. A, 2018, 6, 20056

Enhanced storage ability by using a porous pyrrhotite@N-doped carbon yolk–shell structure as an advanced anode material for sodium-ion batteries†

Ganesh Kumar Veerasubramani,[a] Yuvaraj Subramanian,[a] Myung-Soo Park,[a] Goli Nagaraju,[b] Baskar Senthilkumar,[c] Yun-Sung Lee[d] and Dong-Won Kim*[a]

Received 11th July 2018
Accepted 18th September 2018

DOI: 10.1039/c8ta06667a

rsc.li/materials-a

Sodium-ion batteries (SIBs) are undoubtedly the most promising alternatives to lithium-ion batteries considering the natural abundance, distribution and cost of sodium resources. Still, SIBs face challenges in the development of suitable anode materials due to the large volume change during sodiation/de-sodiation, which results in inferior cycling stability. Herein, we synthesized a yolk–shell structured pyrrhotite ($Fe_{1-x}S$)@N-doped carbon (FS@NC) through a solution-based method and investigated its electrochemical properties for use in SIBs as an anode material. The optimized yolk–shell structured FS@NC with distinctive voids and a core exhibited a high reversible capacity of 594 mA h g^{-1} over 100 cycles at 100 mA g^{-1}, excellent rate capability and superior cycling performance compared to core–shell and pristine $Fe_{1-x}S$ materials. During the charge and discharge cycles, the synergistic effect of the porous core ($Fe_{1-x}S$) with empty voids and a defective carbon shell configuration provided a large electrode/electrolyte contact area and shortened the diffusion path for electrons and sodium ions. It also mitigated the structural degradation by accommodating the volume change during continuous cycles, which was confirmed by *ex situ* SEM and TEM analyses. To demonstrate a practical application, we assembled a sodium-ion full cell with an O3-type $NaCo_{0.5}Fe_{0.5}O_2$ cathode and a yolk–shell structured FS@NC anode, and the results showed superior energy storage performance.

Introduction

Lithium-ion batteries (LIBs) are pervasive in our daily life and have evolved into the dominant power sources for various applications such as portable electronic devices, electric vehicles and large-scale energy storage systems since their discovery in 1991 due to their high energy density and excellent cycling stability.[1,2] Nevertheless, LIBs have drawbacks such as limited lithium resources in the earth's crust and the presence of an uneven distribution of Li deposits. Therefore, increasing cost will be a critical problem for the development of large-scale energy storage systems in the future. Sodium-ion batteries (SIBs) have attracted great attention because Na^+ ions have similar electrochemical properties to Li^+ ions; thus the available design of LIBs could have been promptly used to hasten the research on SIBs.[3–6] In addition, SIBs are suitable alternatives to address all the above issues due to the wide availability of sodium resources in the earth's crust.[7] Thus, a lot of efforts have been devoted for developing SIBs over the past few years.[8–10] However, such SIBs experience severe volume changes due to the large ionic radius of Na^+ (1.02 Å), which restrains the capacity, rate capability and cycling stability of SIBs. Consequently, the development of electrode materials with long-term stability, high capacity and good rate capability is critical.[7,11]

Currently, transition metal chalcogenides have attracted much attention as anode materials due to their impressive energy storage ability, vast abundance, environmental friendliness and high safety.[12–21] Among them, Fe-based chalcogenides, especially iron sulfides, have received much attention due to their availability in nature, low cost and high theoretical capacity. Nevertheless, use of SIBs with iron sulfides has been hampered in real applications due to their sluggish kinetics, low conductivity, sulfur dissolution and large volume changes during continuous sodiation/de-sodiation cycles.[22–27] Many studies have been performed to improve the electrochemical

---

[a] *Department of Chemical Engineering, Hanyang University, Seoul 04763, Republic of Korea. E-mail: dongwonkim@hanyang.ac.kr; Fax: +82 2 2298 4101; Tel: +82 2 2220 2337*

[b] *Department of Chemical Engineering, Kyung Hee University, Gyeonggi-do 17104, Republic of Korea*

[c] *Materials Research Centre, Indian Institute of Science, C.V. Raman Avenue, Bangalore, India*

[d] *Faculty of Chemical Engineering, Chonnam National University, Gwangju 61186, Republic of Korea*

† Electronic supplementary information (ESI) available. See DOI: 10.1039/c8ta06667a

properties of such iron sulfides. The reaction kinetics of active materials could be enhanced and the volume changes during continuous cycles could be mitigated by designing nanostructured active materials. For example, sodium-ion diffusion, cycling stability and rate capability could be greatly improved by anchoring FeS_2 on reduced graphene oxide nanosheets.[28] Carbon-coated FeS maintained a reversible capacity of 365 mA h g^{-1} after 100 cycles at 0.15C.[29] Cobalt-doped FeS_2 nanospheres delivered a discharge capacity of 220 mA h g^{-1} even after long cycles at 2000 mA g^{-1}.[30] It is well known that non-stoichiometric iron sulfide (pyrrhotite, $Fe_{1-x}S$) could provide attractive electrochemical performance due to the Fe vacancy in its octahedral sites. Li *et al.* reported that a nanostructured $Fe_{1-x}S$ anode material exhibited a discharge capacity of 563 mA h g^{-1} over long cycles at 100 mA g^{-1}.[31] Xiao *et al.* reported that the CNT-encapsulated $Fe_{1-x}S$ could deliver a high capacity of 449.2 mA h g^{-1} over long cycles at 500 mA g^{-1}.[32] However, the electrochemical performance needs to be tuned by constructing novel architectures. One interesting system that has gained considerable attention is Co_9S_8/MoS_2 yolk–shell nanostructured spheres for advanced energy storage, which have intriguing characteristics that are not feasible in their solid counterparts.[33] High discharge capacity and improved reaction kinetics could be achieved due to the benefits of shorter diffusion length and improved active sites provided by the yolk–shell architectures, which resulted in an enhanced energy and power density.[34,35] In addition to the benefits mentioned above, the yolk–shell nanostructures can also provide an optimized core–void–shell architecture to endure the severe volume changes encountered due to sodiation/de-sodiation during continuous discharge/charge cycles.[36] The presence of nitrogen atoms in the carbon shell has many advantages such as enhancing the electronic conductivity of the material, improving the wettability of the electrode, introducing more reactive sites and defects for Na^+ ions. All these factors synergistically contribute to an enhanced sodium storage ability, excellent cycling stability and high rate capability for high performance SIBs.[37,38]

Considering all the aspects mentioned above, we designed and synthesized a porous pyrrhotite core encapsulated by a nitrogen-doped carbon shell (FS@NC) as an effective anode material for SIBs in this study. Here, the introduction of nitrogen creates defects within the carbon material, which provides numerous active sites and enhances the electronic conductivity. The acid etching of the $Fe_{1-x}S$ core both creates void space between the core and shell and forms pores inside the core, leading to an improved surface area, accommodating the volume change of the inner active material and promoting sodium ion diffusion.

Experimental details

Materials

Ferrous chloride ($FeCl_2$), 25% aqueous ammonia (NH_4OH), dopamine hydrochloride ($C_8H_{11}NO_2\cdot HCl$), tris-buffer solution and thioacetamide (C_2H_5NS) were purchased from Sigma Aldrich. Carboxyl methyl cellulose binder, *N*-methyl-2-pyrrolidone (NMP, C_5H_9NO), hydrochloric acid (HCl) and ethanol were received from Daejung Chemicals Ltd. De-ionized (DI) water (resistivity: ∼18.0 MΩ cm) was obtained from a Milli-Q water purification system and used throughout experiments.

Preparation of Fe_2O_3 nanoparticles

0.1 g of ferrous chloride was added to 70 mL of ethanol and kept stirring for few hours. Then, 25% aqueous ammonia was added into the solution dropwise until the color changes to dark wine. Afterwards, the solution was transferred to the Teflon-lined autoclave covered with a stainless steel body and maintained at 170 °C for 4 h. The autoclave chamber was gradually cooled down to room temperature. Subsequently, the precipitate was collected and washed with distilled water and ethanol several times using centrifugation, and it was dried at 80 °C for 12 h in a convection oven.

Synthesis of Fe_3O_4@N-doped carbon core–shell

200 mg of prepared Fe_2O_3 nanoparticles and 80 mg of dopamine hydrochloride were dispersed into 100 mL of tris-buffer solution with magnetic stirring for 5 h. The resulting product was collected *via* centrifugation and washed with deionized water and ethanol several times and dried at 70 °C for 12 h in a convection oven. The obtained Fe_2O_3@PDA core–shell particles were transferred to an alumina boat and kept at 500 °C for 3 h under an argon atmosphere at a ramping rate of 5 °C min^{-1} to obtain the Fe_3O_4@NC core–shell particles.

Preparation of Fe_3O_4@NC yolk–shell

The prepared Fe_3O_4@NC core–shell particles were dispersed in 4.0 M HCl solution and stirred for different times (20, 40 and 60 min). Fe_3O_4 was etched in an acidic medium to form the yolk–shell structure. The resulting product was collected *via* centrifugation and washed with deionized water and ethanol three times. It was then dried at 70 °C for 12 h in a convection oven.

Synthesis of $Fe_{1-x}S$@NC yolk–shell

The prepared Fe_3O_4@NC yolk–shell particles were mixed with thioacetamide (1 : 3 weight ratio) and transferred to an alumina boat. The sample loaded on the alumina boat was transferred to a tube furnace for sulfurization. The reaction took place under an argon atmosphere at 500 °C for 5 h. The same procedure was followed to prepare pristine $Fe_{1-x}S$ by direct sulfurization of Fe_2O_3 with thioacetamide.

Characterization and measurements

The crystal structure was identified by powder X-ray diffraction using an X-ray diffractometer (D8 Bruker) with Cu Kα radiation (λ = 1.5405 Å) in the scan range (2θ) of 10–100°. Rietveld refinement of the XRD pattern was performed using a general structure analysis system (GSAS) to determine the detailed structural information. The nature of the chemical bonds was investigated by Raman spectroscopy (Dongwoo optron, MonoRa 780i). The morphologies of the prepared samples were investigated using a scanning electron microscope (NOVA Nano SEM-450) equipped with energy dispersive spectroscopy (EDS). A high-resolution transmission electron microscope (HRTEM, JEOL, JEM 2100F) and elemental mapping were used to observe the morphology of the prepared materials. X-ray photoelectron spectroscopy (XPS) was performed with a spectrometer having Mg/Al Kα radiation (XPS, VG Multilab ESCA System, 220i). Cyclic voltammetry (CV) and electrochemical impedance spectroscopy were performed using a CH instrument (CHI600D Electrochemical Workshop). The charge and discharge cycling test was carried out using battery test equipment (WBCS 3000, WonA Tech Co., Ltd.) at 25 °C.

Electrode preparation and full cell assembly

The viscous slurry was prepared by grinding active materials ($Fe_{1-x}S$, 70 wt%) with Super-P carbon (15 wt%) and carboxy methyl cellulose binder (15 wt%) using water. The electrode was prepared by coating the slurry onto the Cu foil and drying in a vacuum oven at 110 °C for 12 h. The active mass loading in the electrode was about 3.0 mg cm^{-2}. To evaluate the electrochemical performance of the electrode, a CR2032-type coin cell was assembled by sandwiching a glass fiber separator (Whatman CAT no. 1823-047) between sodium foil (Alfa Aesar 99%) and the prepared electrode. A liquid electrolyte with 1.0 M $NaClO_4$ in ethylene carbonate (EC)/propylene carbonate (PC) (50 : 50 by volume, battery grade) containing 10.0 wt% fluoroethylene carbonate (FEC) as an additive was kindly supplied by PANAX ETEC Co. Ltd. and was used as received. Karl Fischer titration using a Mettler-Toledo Coulometer confirmed that the water content in the liquid electrolyte was less than 20 ppm. $NaCo_{0.5}Fe_{0.5}O_2$ cathode was prepared by casting NMP-based slurry consisting of $NaCo_{0.5}Fe_{0.5}O_2$ (80 wt%), Super-P carbon (10 wt%) and poly(vinylidene fluoride) binder (10 wt%) onto the Al foil. The resulting electrode was dried in a vacuum oven at 110 °C for 12 h. A sodium-ion full cell was assembled with a yolk–shell structured $Fe_{1-x}S$@NC-40 anode and a $NaCo_{0.5}Fe_{0.5}O_2$ cathode using the same electrolyte and separator used in the half-cell assembly. The mass ratio of active materials in the anode to those in the cathode has been optimized to 1.0 : 4.3 to obtain the best cycling performance. All the cells

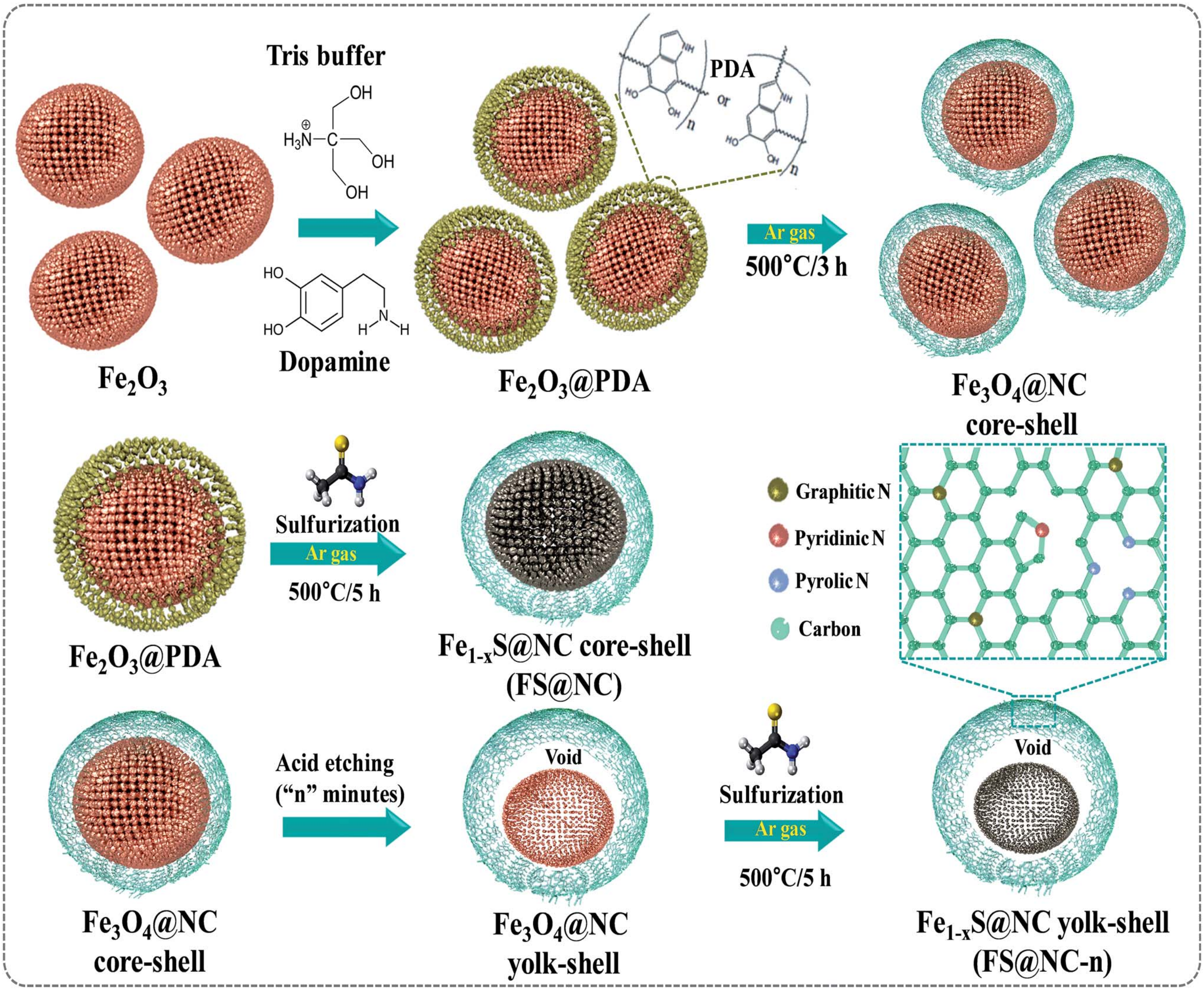

Fig. 1 Schematic illustration of the preparation of the yolk–shell structured FS@NC and FS@NC-*n* particles.

were assembled inside a glove box under an argon atmosphere and electrochemical measurements were carried out at 25 °C.

Results and discussion

An effective approach was used to enhance the Na-ion storage and cycling stability of the anode material by designing yolk–shell structured nanocomposites with a large surface area and high conductivity. Herein, we facilely designed the selective etching of N-doped carbon encapsulated $Fe_{1-x}S$ nanoparticles to form yolk–shell nanoarchitectures ($Fe_{1-x}S$@NC), as schematically illustrated in Fig. 1. Firstly, the Fe_2O_3 nanoparticles were prepared by a hydrothermal technique using ferrous chloride ($FeCl_2$) as a starting precursor. $FeCl_2$ was reacted with an ammonium hydroxide solution under controlled pH to yield a brown color solution. Under hydrothermal treatment, the solution was converted to iron oxide (Fe_2O_3) nanoparticles. Subsequently, the *in situ* chemical polymerization of Fe_2O_3 with dopamine was carried out to obtain polydopamine-coated Fe_2O_3 (Fe_2O_3@PDA), which further underwent an annealing treatment under an inert atmosphere to obtain Fe_3O_4 particles encapsulated by nitrogen-doped carbon (Fe_3O_4@NC). Afterwards, the Fe_3O_4@NC nanoparticles were subjected to partial etching of the Fe_3O_4 core using HCl, followed by sulfurization to form yolk–shell structured $Fe_{1-x}S$@NC-*n* (*n* in $Fe_{1-x}S$@NC-*n* means the etching time in units of min). These kinds of

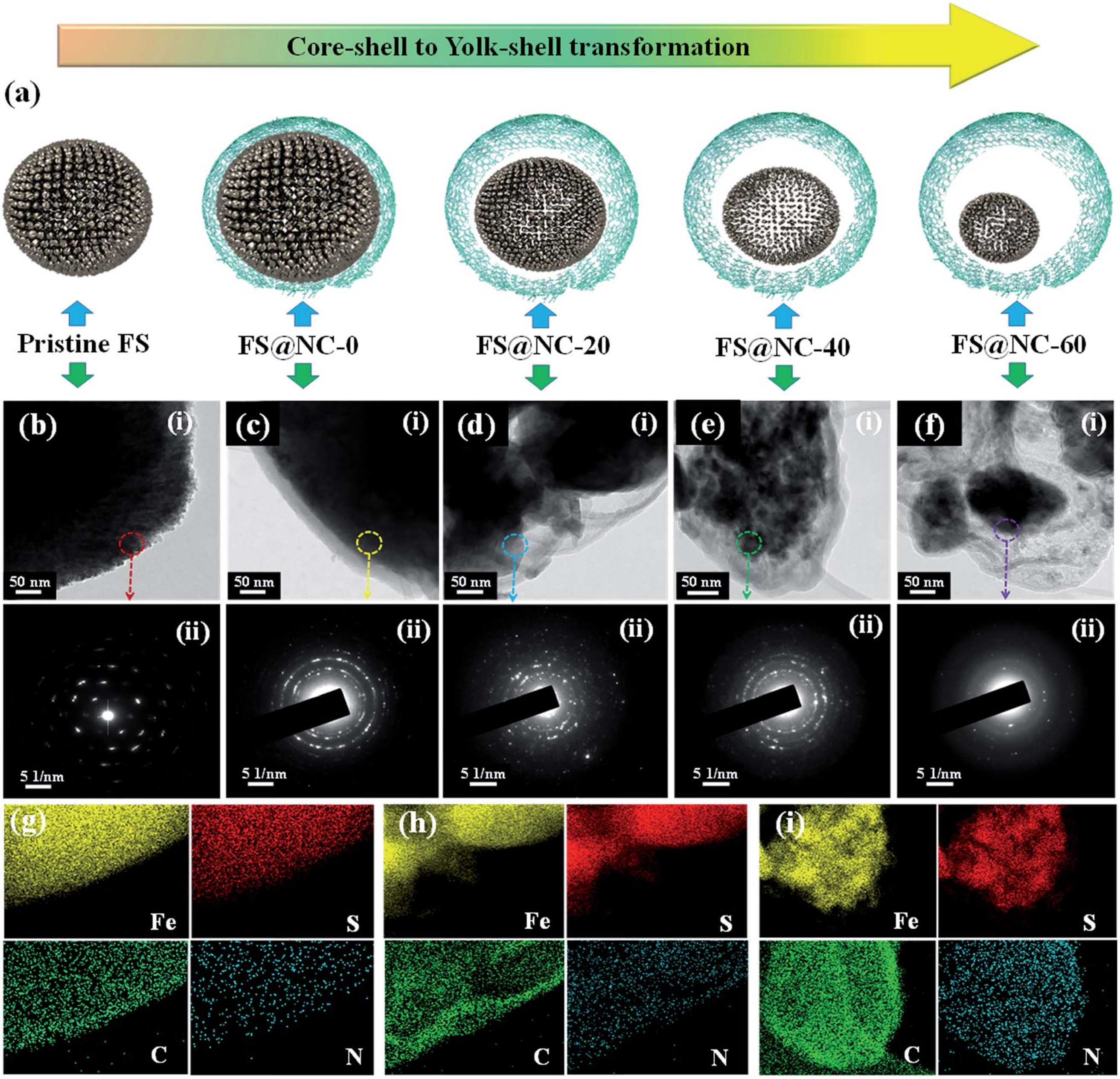

Fig. 2 (a) Structural evolution of the FS@NC core–shell to FS@NC yolk–shell with respect to the etching time. TEM images of (b) pristine FS, (c) FS@NC-0, (d) FS@NC-20, (e) FS@NC-40 and (f) FS@NC-60. Elemental mapping images of (g) FS@NC-0, (h) FS@NC-20 and (i) FS@NC-40.

nanoarchitectures can provide high surface area, which enables efficient pathways for Na-ion penetration. We also prepared the core–shell structured $Fe_{1-x}S$@NC by the direct sulfurization of Fe_3O_4@PDA with thioacetamide. The morphologies of the prepared samples were examined using field-emission scanning electron microscopy (FE-SEM) and transmission electron microscopy (TEM). The spherical shaped morphology was observed for the hydrothermally prepared Fe_2O_3, as can be seen in Fig. S1.† A FE-SEM image of Fe_3O_4@NC particles is also shown in Fig. S2.† After acid etching and subsequent sulfurization, the structural evolution of $Fe_{1-x}S$@NC with core–shell to yolk–shell transformation under different etching times is schematically illustrated in Fig. 2(a). Fig. 2(b), S3 and S4† show the FE-SEM and TEM images of the pristine $Fe_{1-x}S$ (*i.e.*, without NC coating) material. After sulfurization, slight changes from the spherical-like particles to random nanoparticles were observed for pristine $Fe_{1-x}S$ particles. Also, the SAED pattern in Fig. 2(b)(ii) shows clear ring pattern spots, indicating the polycrystalline nature of the FS nanoparticles. The core–shell-like structure was clearly observed after coating the nitrogen-doped carbon (NC) on the FS particle, as presented in Fig. 2(c) and S5.† Here, NC coated on FS was formed by the polymerization of dopamine, followed by carbonization under an inert atmosphere. About 25 nm of the NC layer was uniformly coated on the surface of the FS. The FS@NC particles were subjected to acid etching for different times to obtain the yolk–shell

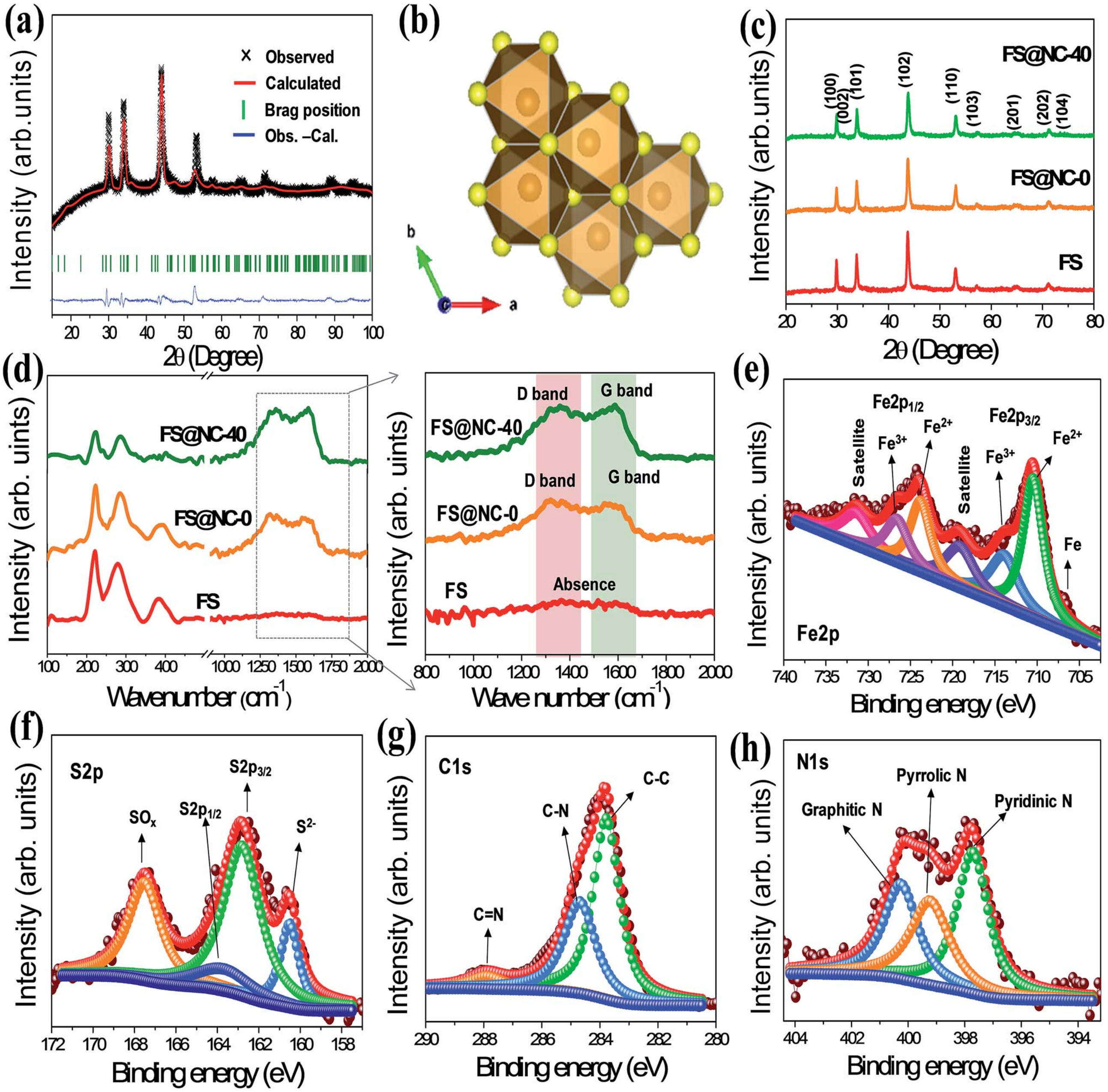

Fig. 3 (a) XRD refinement and (b) the crystal structure of pristine FS. (c) XRD patterns and (d) Raman spectra of FS, FS@NC-0 and FS@NC-40. XPS spectra of the (e) Fe2p core-level, (f) S2p core-level, (g) C1s core-level and (h) N1s core-level of FS@NC-40.

structured FS@NC-*n* with optimum void space. Here, FS@NC-0 represents the FS@NC core–shell particles without etching. Fig. 2(d)–(f) and S6–S8† show the TEM images and SAED patterns of the prepared FS@NC-20, FS@NC-40 and FS@NC-60, respectively. It is apparent from the TEM images that the void space increases as the etching time increases. The images show both void space between the carbon layer and the FS core, and the porous FS inside the particle, which is beneficial for achieving the enhanced electrochemical performance. The FS@NC-60 particle exhibited the largest void space between the FS core and the carbon layer. Fig. S6–S8† show the TEM images of the FS@NC-20, FS@NC-40 and FS@NC-60 particles at different magnifications. The SAED pattern of FS@NC-60 (*i.e.*, after sulfurization) shows the polycrystalline nature with imperceptible rings, because the NC layer diminishes the bright FS rings. Fig. 2(g)–(i) present the elemental mapping images of FS@NC-0, FS@NC-20 and FS@NC-40, respectively. Fig. 2(g) shows that all the elements such as Fe, S, C and N are uniformly distributed. Interestingly, the partial etching created the void space as observed from the TEM images, and the outer coating layer was distributed by carbon and nitrogen. While the FS core can deliver a high capacity, the N-doped carbon layer can improve the electrical conductivity, and the void space can accommodate the volume changes during the repeated sodiation/de-sodiation cycles.

The structural and crystalline properties of the synthesized materials were characterized by X-ray diffraction (XRD) analysis. Fig. S9† shows the XRD pattern of the prepared Fe_2O_3 nanoparticles, which corresponds the rhombohedral crystal structure and all the peaks were well matched to the JCPDS card no. 89-2810. Also, the XRD pattern of Fe_3O_4@NC in Fig. S10† presents the well-defined peaks at 30.1°, 35.5°, 43.1°, 53.5°, 56.9°, 62.7° and 74.0°, where all the diffraction peaks can be indexed with the cubic phase and matched with the JCPDS card no. 19-0629. The oxidation states of Fe in Fe_3O_4 plays a major role in formation of iron deficient pyrrhotite particles. Unlike the Fe_2O_3, the cubic phase of Fe_3O_4 contains both Fe^{2+} and Fe^{3+} ions. Here, Fe^{2+} ion occupies the octahedral site, whereas the Fe^{3+} ion occupies both octahedral and tetrahedral sites evenly, which is responsible for the non-stoichiometric nature of $Fe_{1-x}S$. Fig. 3(a) shows the XRD refinement of pristine FS after sulfurization of Fe_3O_4 with thioacetamide. All the diffraction peaks can be assigned to $Fe_{1-x}S$ with a hexagonal phase without any peaks for other phases or impurities. The peaks at 29.8°, 31.3°, 33.8°, 43.8°, 53.1°, 57.4°, 65.2°, 71.1° and 74.5° correspond to the (100), (002), (101), (102), (110), (103), (201), (202) and (104) crystal planes, respectively.[39] Fig. 3(b) presents the crystal structure according to the $Fe_{1-x}S$ refinement data. As shown, Fe ions reside in the octahedral sites, whereas the S ion occupies the trigonal prismatic site. Fig. 3(c) compares the XRD patterns of pristine FS, FS@NC-0 and FS@NC-40 (see Fig. S11† for FS@NC-20, FS@NC-60). The hexagonal phase of FS could be achieved even under severe processing conditions such as high temperature carbonization, acid etching and high temperature

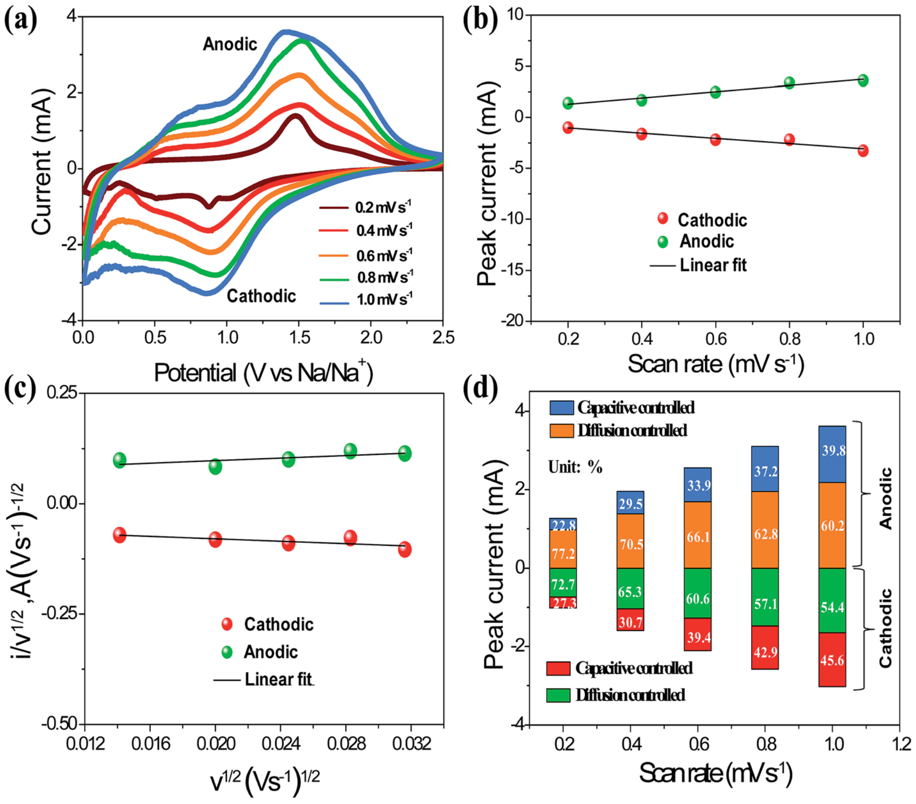

Fig. 4 Kinetic investigation of the prepared FS@NC-40 electrodes. (a) *CV* curves at different scan rates ranging from 0.2 to 1 mV s^{-1}, (b) linear plot of scan rate *vs.* peak current, (c) linear plot between $v^{1/2}$ *vs.* $iv^{-1/2}$, and (d) relative contribution of the capacitive- and diffusion-controlled processes with respect to the scan rate.

sulfurization. No peaks for carbon were observed apart from the slight decrease in the intensity of each (*hkl*) plane; this reveals that the coated carbon is amorphous.[40] Raman spectra in Fig. 3(d) present three bands at low wavenumbers, which correspond to pyrrhotite.[41] After coating N-doped carbon on the surface of FS, two peaks appear at 1345 and 1570 cm^{-1}, which are related to the disordered carbon (D band) and graphitic carbon (G band), respectively. This result further confirms the presence of amorphous carbon on the surface of FS. All the peaks in FS@NC-40 slightly shift to a higher wavenumber, which might be due to many factors such as the synthesis method, morphology of the material, crystal size, degree of the structural order and the energy of interaction between the ions.[42] Furthermore, X-ray photoelectron spectroscopy (XPS) was performed to identify the chemical composition and valence states of the FS@NC-40, and the results are presented in Fig. 3(e)–(h). As shown in Fig. 3(e), the high resolution Fe2p core-level spectrum showed two major regions, Fe2p$_{3/2}$ and Fe2p$_{1/2}$. Here, the peaks observed at 710.5 and 723.9 eV correspond to Fe^{2+}, whereas those at 714.1 and 726.7 eV indicate the presence of Fe^{3+} in the FS@NC-40 yolk–shell material.[32,43] Two more peaks were observed as the satellite peaks. The broad peaks at 163.8 and 162.6 eV in Fig. 3(f) can be attributed to S2p$_{1/2}$ and S2p$_{3/2}$, respectively. The peak at the high binding energy indicates the presence of oxidized groups (SO$_x$).[44] The C1s core-level spectrum can be deconvoluted into three peaks at binding energies of 283.8, 284.7 and 287.9 eV, which correspond to the C–C, C–N, C═N bonds, respectively (Fig. 3(g)). The N1s core-level spectrum in Fig. 3(h) can be resolved into three major peaks at binding energies of 397.7, 399.3 and 400.3 eV, which are attributed to the pyridinic-N, pyrrolic-N and graphitic-N bonds, respectively.[45] Further, the elemental contents of the prepared materials were analyzed using the EDS analysis and the results are presented in Fig. S12.† As shown in these figures, the etching of the inner Fe$_{1-x}$S core led to a gradual decrease in Fe and S contents, whereas the contents of carbon and nitrogen gradually increased with the etching time. According to the TGA analysis, the amount of carbon was calculated to be 15.2, 18.8, 21.9 and 33.6 wt% for FS@NC-0, FS@NC-20, FS@NC-40 and FS@NC-60, respectively.

The electrochemical performance of the obtained electrodes was investigated. Fig. 4(a) presents the CV curves of the FS@NC-40 electrode at different scan rates ranging from 0.2 to 1 mV s^{-1}. A pair of redox peaks (cathodic and anodic) was observed at

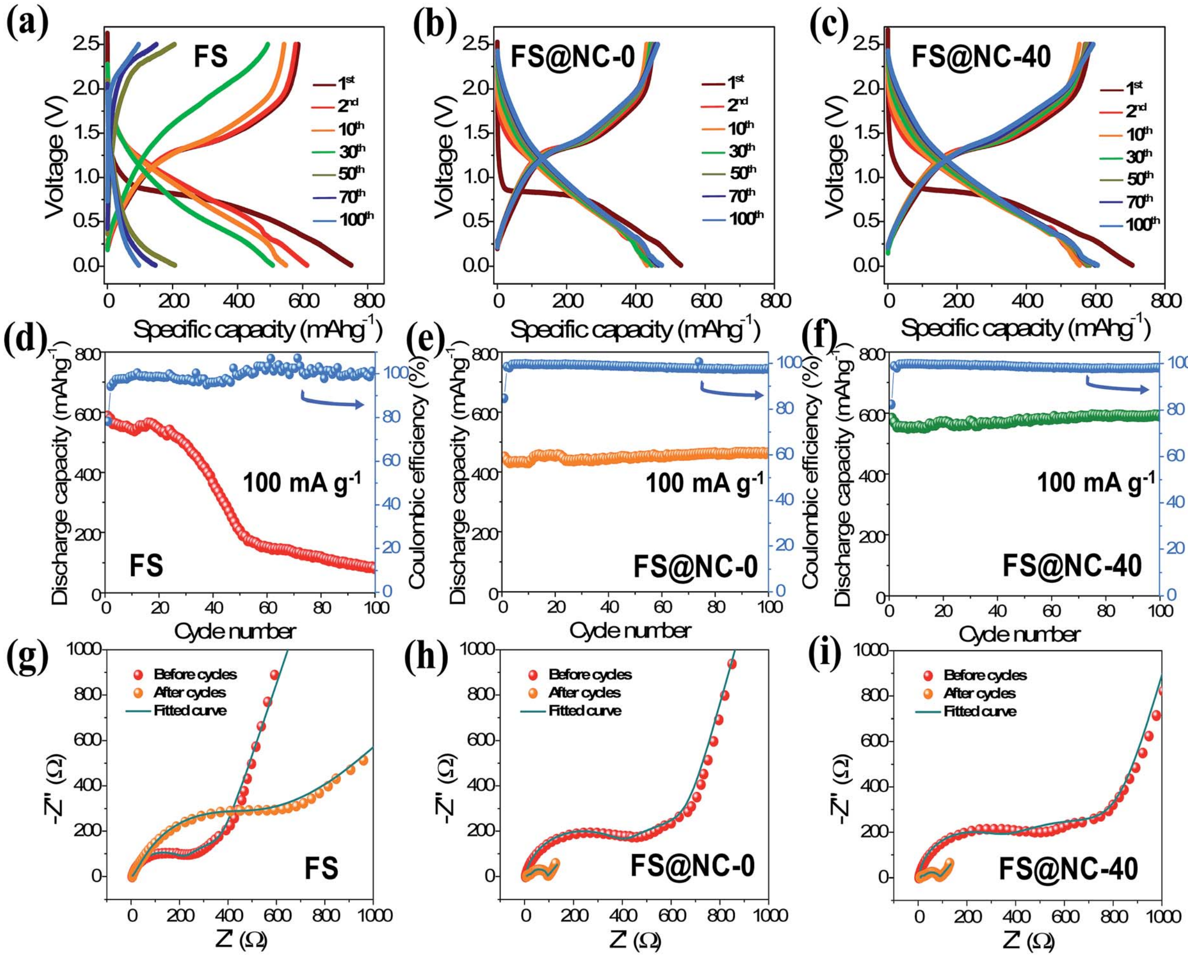

Fig. 5 Charge and discharge curves of the (a) FS, (b) FS@NC-0 and (c) FS@NC-40 electrodes at 100 mA g^{-1}. Cycling performance of the (d) FS, (e) FS@NC-0 and (f) FS@NC-40 electrodes at 100 mA g^{-1}. AC impedance spectra of the (g) FS, (h) FS@NC-0 and (i) FS@NC-40 electrodes before and after the cycles.

each scan rate. The power law was applied to differentiate the relative contributions of the diffusion and capacitive-controlled capacity to the total charge. As shown in Fig. 4(b), the peak current can be expressed as a function of the scan rate, $i_p = a \times \nu^b$, where i_p is the peak current (A), ν is the scan rate, a and b are the adjustable parameters.[46] On increasing the scan rate, the peak shape was well maintained even at a high scan rate, demonstrating the good electrochemical reversibility of the material. The calculated "b" values for the cathodic and anodic peaks were 0.64 and 0.67, respectively, which belong to the transitional area between the capacitive and diffusion-controlled behavior.[47] Fig. S13† reveals a linear plot between the peak current *vs.* square root of the scan rate for cathodic and anodic processes of the FS@NC-40 electrode. To evaluate the charge storage behavior, the power law can be modified into the following relation,

$$i_p = k_1\nu + k_2\nu^{1/2} \quad (1)$$

where $k_1\nu$ and $k_2\nu^{1/2}$ are the current contributions from non-faradaic and faradaic processes. The values of the slope and intercept from the linear fit of the plot between $i_p/\nu^{1/2}$ *vs.* $\nu^{1/2}$ represent k_1 and k_2, respectively (Fig. 4(c)). The contribution of capacitive- and diffusion-controlled processes could be calculated from the above equation, as depicted in Fig. 4(d). At low scan rates, the contribution of diffusion-controlled process dominates the charge storage capacity. The diffusion-controlled process decreases on increasing the scan rate, and the capacitive-controlled process gradually increases. The unique structural characteristics and large surface area may partially account for this enhanced capacitive contribution. Fig. 5(a) shows the voltage profiles of the pristine FS electrode in the voltage range of 0.01 to 2.50 V at a current density of 100 mA g^{-1}. A high irreversible capacity of 22% was observed due to the formation of a solid electrolyte interphase (SEI) layer in the first cycle. A reversible capacity of 607 mA h g^{-1} was obtained in the first cycle. However, a drastic decline in the capacity was

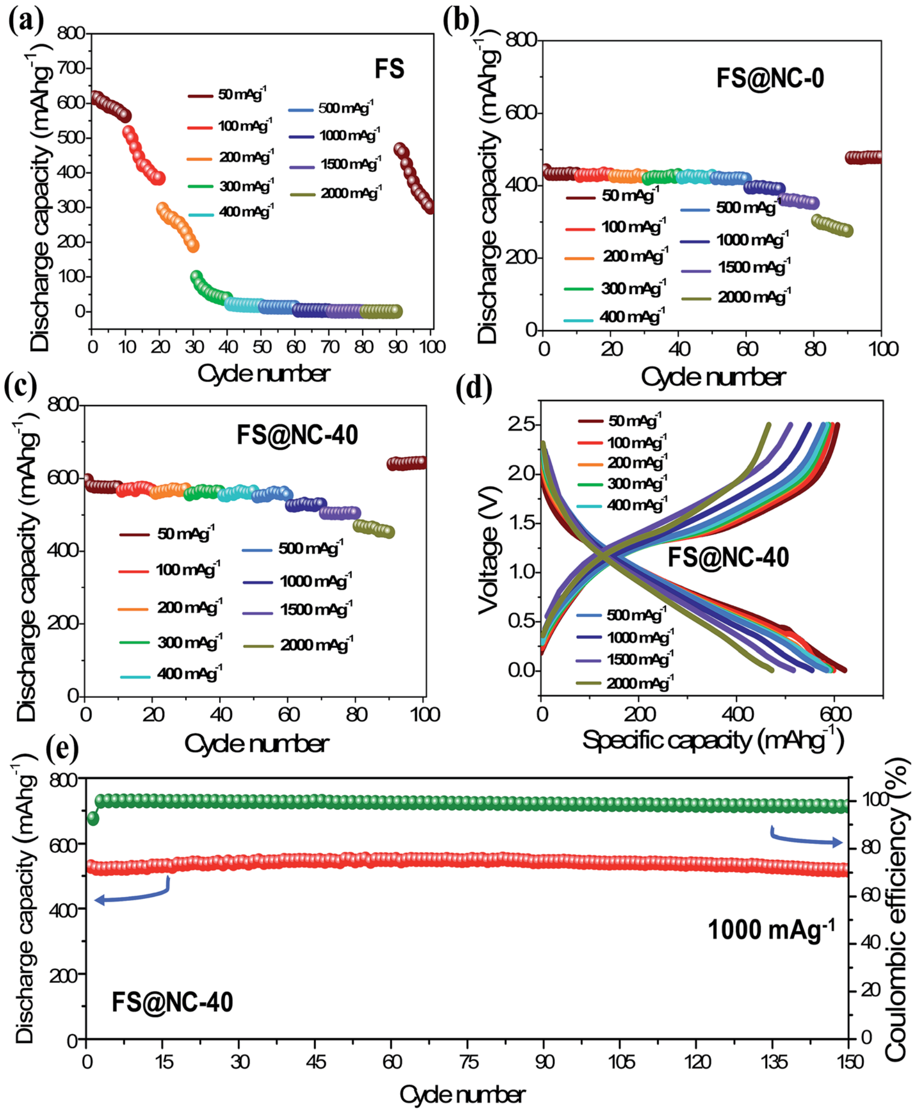

Fig. 6 Rate capability of the (a) FS, (b) FS@NC-0 and (c) FS@NC-40 electrodes. (d) Charge and discharge curves of the FS@NC-40 electrode at different current densities ranging from 50 to 2000 mA g^{-1}. (e) Cycling stability of the FS@NC-40 electrode at a current density of 1000 mA g^{-1}.

observed for extended cycling. The cycling stability was greatly improved in the case of FS@NC-0 (Fig. 5(b)), although the initial capacity decreased. The FS@NC-40 electrode in Fig. 5(c) exhibits an enhanced discharge capacity of 594 mA h g^{-1} with the help of the yolk–shell architecture. Fig. 5(d)–(f)present the cycling performance for pristine FS, FS@NC-0 and FS@NC-40 electrodes, respectively (see Fig. S14 in ESI† for FS@NC-20 and FS@NC-60 electrodes). The pristine FS electrode in Fig. 5(d) shows a large capacity fading due to the large volume change in the $Fe_{1-x}S$ electrode during continuous sodiation/de-sodiation. The capacity fading can be suppressed by coating N-doped carbon over the $Fe_{1-x}S$ material, as shown in Fig. 5(e). Fig. 5(f) depicts the cycling performance of the FS@NC-40 electrode with an improved initial coulombic efficiency of 82.4%. This value is slightly low when compared to the FS@NC-0 electrode, which can be attributed to the increased surface area of the FS@NC-40 yolk–shell electrode *via* a core–void–shell architecture. Fig. S15† shows the cycling performance of various electrodes at a high current density of 1000 mA g^{-1}. Among the electrodes investigated, the FS@NC-40 electrode exhibited the best cycling performance in terms of initial discharge capacity and cycling stability. The electrochemical performance of

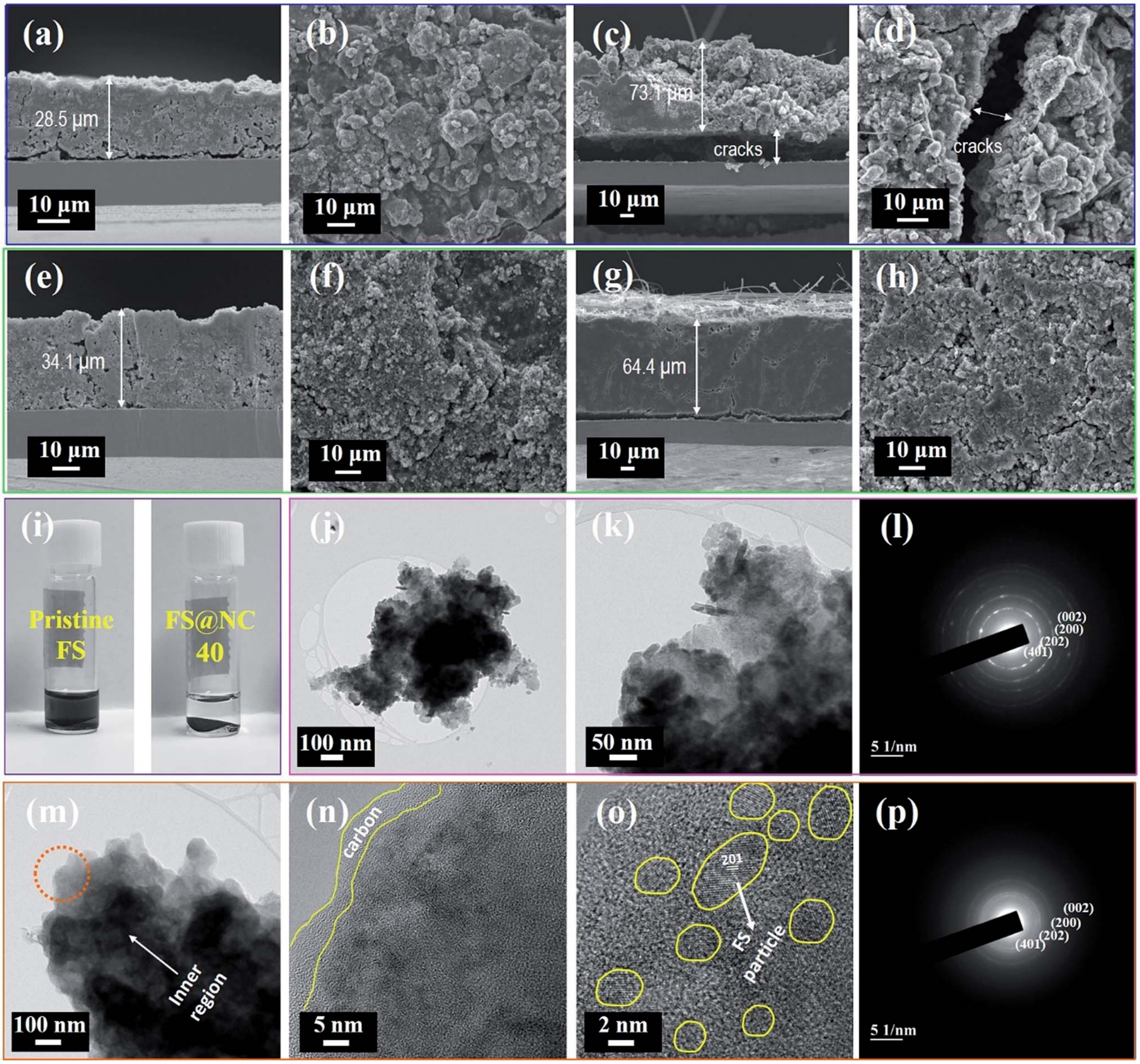

Fig. 7 FE-SEM images of (a) cross-section and (b) surface of the pristine FS electrode before cycling, (c) cross-section and (d) surface of the pristine FS electrode after cycles. FE-SEM images of (e) cross-section and (f) surface of the FS@NC-40 electrode before cycling, (g) cross-section and (h) surface of the FS@NC-40 electrode after cycles. (i) Photo images of the pristine FS and FS@NC-40 electrodes after cycles with sonication in ethanol. (j and k) TEM images at different magnifications and (l) the SAED pattern of the pristine FS electrode after cycles. (m and n) TEM images at different magnifications, (o) HR-TEM image and (p) SAED pattern of the FS@NC-40 electrode after cycles.

different electrodes was further investigated by AC impedance measurements before and after cycling, and the resulting AC impedance spectra are shown in Fig. 5(g)–(i). All the electrodes showed a depressed semicircle in the high and medium frequency regions, whereas a straight line was observed in the low frequency region. A high-frequency intercept of the real axis is attributed to the electrolyte resistance (R_e), and the overlapped semicircle in the high to middle frequency range arises from the resistance due to Na^+ ion migration through the surface film formed on the electrode (R_{sf}) and charge transfer reaction at the electrode–electrolyte interface (R_{ct}), and finally the low frequency region is related to the sodium ion diffusion within the electrode. These spectra could be fitted by using the equivalent circuit given in Fig. S16.† The R_e values were slightly increased for all the electrodes after cycling. On the other hand, there was a drastic increase in R_{sf} and R_{ct} with cycling in the pristine FS electrode, which can be attributed to the loss of conductivity of the electrode by severe volume change and occurrence of cracks within the pristine FS electrode.[48] In contrast, both R_{sf} and R_{ct} were decreased after cycling in the FS@NC-0 and FS@NC-40 electrodes, which demonstrated that the coating of N-doped carbon on the $Fe_{1-x}S$ particles improved the conductivity of the electrode and cycling stability. The FS@NC-40 electrode exhibited the lowest R_{ct} after cycling, which can be ascribed to the void–shell architecture with high surface area that accommodates the volume change of the FS core during cycling.

The rate capabilities of the various electrodes were evaluated at different current densities ranging from 50 to 2000 mA g^{-1}. As shown in Fig. 6 and S17,† the FS@NC-40 electrode exhibited the best rate performance among all the electrodes. The discharge capacity of the pristine FS electrode significantly dropped to lower values at high current densities (Fig. 6(a)), whereas the FS@NC-0 electrode exhibited a discharge capacity of 303 mA h g^{-1} (Fig. 6(b)), and the FS@NC-40 electrode delivered a discharge capacity of 470 mA h g^{-1} (Fig. 6(c)) even at a high current density of 2000 mA g^{-1}. These results confirmed that the designed FS@NC-40 electrode exhibited excellent rate capability compared to the pristine and other electrodes. *Ex situ* FE-SEM analyses of the electrodes were performed, and the results are

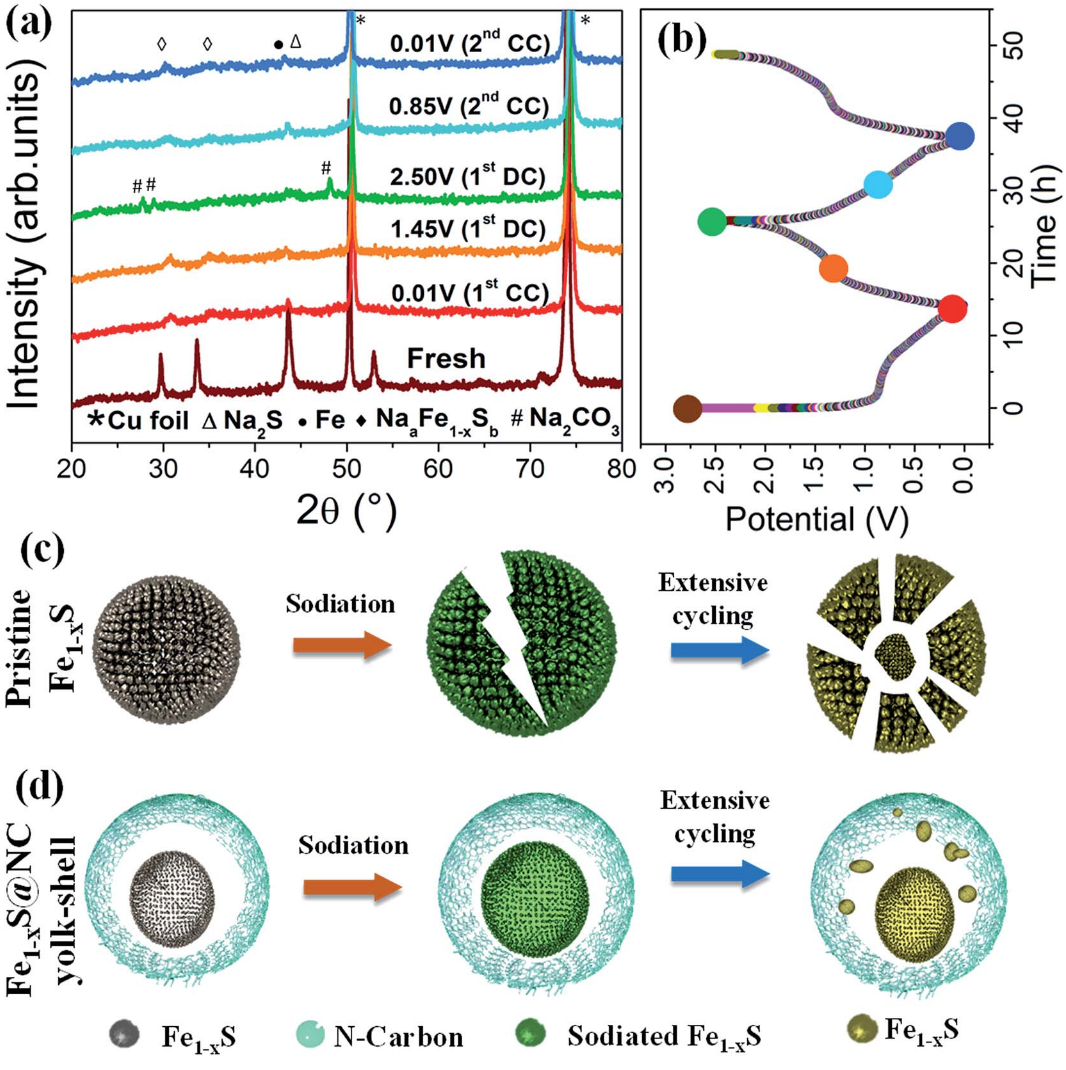

Fig. 8 (a) *Ex situ* XRD patterns of the FS@NC-40 electrode at different electrode potentials and (b) charge and discharge curves for two continuous cycles. A schematic illustration of the sodiation process in the (c) pristine FS and (d) FS@NC-40 yolk–shell electrodes.

presented in Fig. 7(a)–(h). Before cycling, the cross-sectional and surface images of the pristine FS electrode show smooth and uniform morphologies on a Cu current collector. However, the electrode was detached from the current collector and the electrode thickness was significantly increased after cycling due to the volume expansion of the active material with extensive cracking. In contrast, the FE-SEM images of the FS@NC-40 electrode show less volume expansion and little cracks on the surface of the electrode, which demonstrates its excellent volume accommodation and good adhesion to the current collector. The cycled electrodes were immersed into ethanol and kept in a bath with sonication. Fig. 7(i) presents the photo images of the pristine FS and FS@NC-40 electrodes after sonication. Due to the large volume expansion and large cracks on the surface of the electrode, the pristine FS electrode materials were peeled off into the solvent, whereas no dissolution of the electrode materials into the solvent was observed in the FS@NC-40 electrode. Fig. 7(j)–(l) show the TEM images and SAED pattern of the pristine FS electrode material. The structural degradation of the active materials was observed. In contrast, the volume strain on the FS particles in the FS@NC-40 electrode was well controlled by the presence of a void and N-doped carbon shell, as shown in Fig. 7(m) and (n). The HR-TEM image in Fig. 7(o) shows the presence of the FS particle with carbon materials and the SAED pattern in Fig. 7(p) presents the slight cloudy pattern of FS due to the addition of a conducting agent.

The charge storage mechanism was further investigated by performing *ex situ* XRD analysis, and the results are presented in Fig. 8(a) and (b). At open circuit voltage, all the diffraction peaks were related to the $Fe_{1-x}S$, and two additional peaks at 50.3° and 74° correspond to the Cu foil. After sodiation, the sharp peaks completely disappeared, and the obtained results were similar to the previous reports based on metal sulfides, suggesting that a conversion-type reaction occurred. The peaks related to $Fe_{1-x}S$ were not observed at 0.01 V, and the peaks corresponding to sodiated $Fe_{1-x}S$ were subsequently observed around 31° and 35°. In the fully de-sodiated state, three more peaks appeared at 27.6°, 29.0° and 48.2°, which are related to Na_2CO_3. During the process, Fe particles were generated during the conversion reaction, which was confirmed from the peak at 43°.[49] Based on the above results, the sodium storage mechanism for the prepared $Fe_{1-x}S$ materials can be given as follows.

$$\begin{aligned}&Fe_{1-x}S + 2Na^+ + 2e^- \rightarrow\\&\quad Na_2S + Fe;\ Na_2S + Fe \leftrightarrow Na_aFe_{1-x}S_b + 2Na^+ + 2e^- \end{aligned} \qquad (2)$$

A schematic illustration of the sodiation and de-sodiation process for the pristine $Fe_{1-x}S$ and yolk–shell structured $Fe_{1-x}S$@NC-40 electrodes is shown in Fig. 8(c) and (d). The FS particle started to change in volume during continuous cycles, which caused severe structural damage, resulting in poor cycling stability. On the other hand, the FS particle

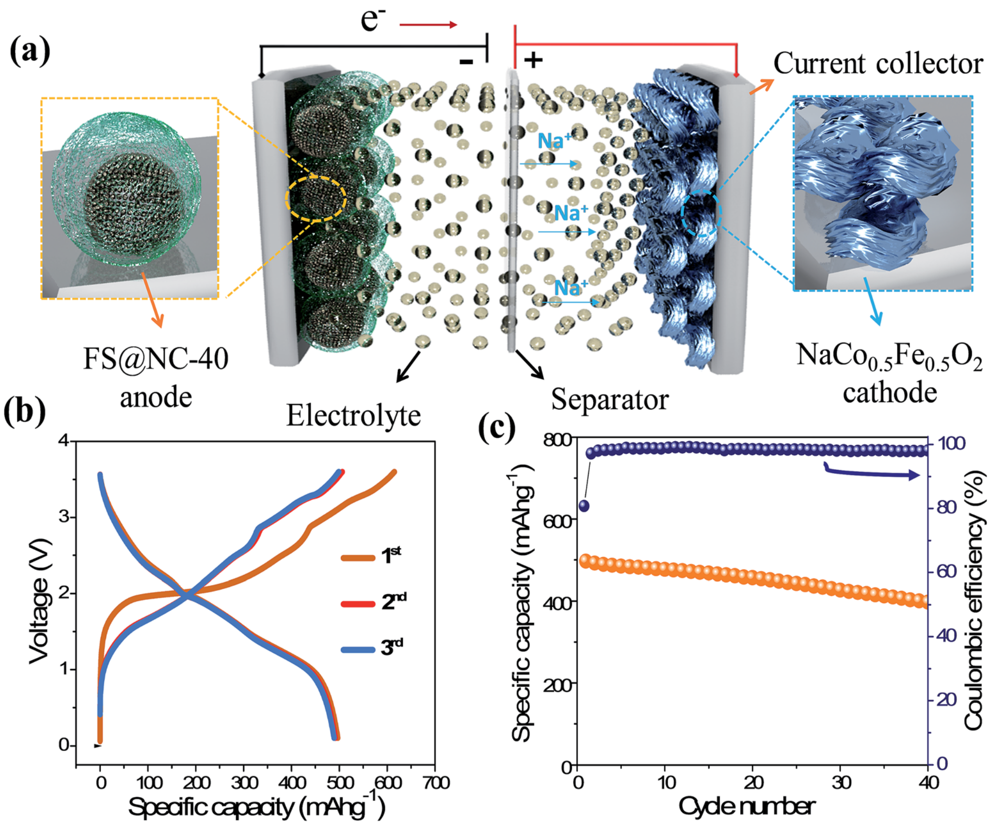

Fig. 9 (a) A sodium-ion full cell assembled with FS@NC-40 anode and $NaCo_{0.5}Fe_{0.5}O_2$ cathode. (b) Charge and discharge curves of the sodium-ion full cell at 50 mA g^{-1} based on the anode material and (c) its cycling performance.

encapsulated by N-doped carbon can control the large volume expansion and provide good cycling stability. The electrochemical performance is compared with the results recently reported on other metal sulfide-based anode materials for SIBs in Table S1 of the ESI.† The benefit of the yolk–shell structured FS@NC-40 material can be explained as follows. First, the N-doped carbon coating on the surface of the $Fe_{1-x}S$ particle improves the electronic conductivity of the electrode. Second, the highly porous nature of the $Fe_{1-x}S$ core inside FS@NC-40 (as compared to the core–shell structured FS@NC-0 particle) provides more active sites and higher surface area. Third, the void space can furnish enough space for buffering the volume expansion of the inner FS core.[50–54]

To explore the practical use of the prepared material as an anode for SIBs, a sodium-ion full cell was assembled with the FS@NC-40 anode and $NaCo_{0.5}Fe_{0.5}O_2$ cathode (see Fig. S18† for cycling performance of the cathode half-cell). Fig. 9(a) shows a schematic illustration of the fabricated full cell. Fig. 9(b) presents the galvanostatic charge and discharge curves of the sodium-ion cell in the voltage range of 0.1 to 3.6 V at a constant current density of 50 mA g^{-1} based on the mass of the FS@NC-40 anode. An initial discharge capacity of 500 mA h g^{-1} was obtained based on the mass of the active FS@NC-40 material. Excellent cycling stability was achieved with negligible loss of specific capacity, as shown in Fig. 9(c). Such a large capacity and good cycling stability are attributed to the superior electrochemical performance of the FS@NC-40 anode and $NaCo_{0.5}Fe_{0.5}O_2$ cathode. Overall, the yolk–shell structured FS@NC-40 material provided attractive electrochemical performance, including high specific capacity, good capacity retention and superior rate capability.

Conclusions

In summary, the yolk–shell structured $Fe_{1-x}S$ encapsulated by N-doped carbon was designed and synthesized for use as an anode material in sodium-ion batteries. The yolk–shell structured FS@NC-40 material exhibited a high discharge capacity of 594 mA h g^{-1} at 100 mA g^{-1}, good cycling stability at low and high current rates and excellent rate capability. The superior performance of the FS@NC-40 yolk–shell electrode was attributed to the fast sodium ion diffusion due to the porous core that provides more active sites, the enhanced electrical conductivity and the efficient accommodation of the volume expansion of the inner $Fe_{1-x}S$ core. It was also demonstrated that the sodium-ion full cell assembled with FS@NC-40 anode and $NaCo_{0.5}Fe_{0.5}O_2$ cathode exhibited good cycling performance in terms of reversible capacity and cycling stability. Our study demonstrates the excellent potential of the $Fe_{1-x}S$@NC yolk–shell material for high performance sodium-ion storage applications.

Conflicts of interest

There are no conflicts to declare.

Acknowledgements

This work was supported by the National Research Foundation of Korea (NRF) funded by the Korean Government (2017R1C1B2012700) and the Basic Science Research Program of NRF, funded by the Ministry of Science, ICT, and Future Planning (2016R1A4A1012224).

References

1 B. Dunn, H. Kamath and J. M. Tarascon, *Science*, 2011, **334**, 928.

2 D. Larcher and J. M. Tarascon, *Nat. Chem.*, 2014, **7**, 19.

3 S. W. Kim, D. H. Seo, X. Ma, G. Ceder and K. Kang, *Adv. Energy Mater.*, 2012, **2**, 710.

4 V. Palomares, P. Serras, I. Villaluenga, K. B. Hueso, J. Carretero-Gonzalez and T. Rojo, *Energy Environ. Sci.*, 2012, **5**, 5884.

5 Y. Fang, Q. Liu, L. Xiao, Y. Rong, Y. Liu, Z. Chen, X. Ai, Y. Cao, H. Yang, J. Xie, C. Sun, X. Zhang, B. Aoun, X. Xing, X. Xiao and Y. Ren, *Chem*, 2018, **4**, 1167.

6 Y. Fang, X.-Y. Yu and X. W. Lou, *Angew. Chem.*, 2017, **56**, 5801.

7 S. P. Ong, V. L. Chevrier, G. Hautier, A. Jain, C. Moore, S. Kim, X. Ma and G. Ceder, *Energy Environ. Sci.*, 2011, **4**, 3680.

8 M. D. Slater, D. Kim, E. Lee and C. S. Johnson, *Adv. Funct. Mater.*, 2013, **23**, 947.

9 N. Yabuuchi, K. Kubota, M. Dahbi and S. Komaba, *Chem. Rev.*, 2014, **114**, 11636.

10 D. Kundu, E. Talaie, V. Duffort and L. F. Nazar, *Angew. Chem., Int. Ed.*, 2015, **54**, 3431.

11 Y. You, X. L. Wu, Y. X. Yin and Y. G. Guo, *Energy Environ. Sci.*, 2014, **7**, 1643.

12 Q. Wang, R. Zou, W. Xia, J. Ma, B. Qiu, A. Mahmood, R. Zhao, Y. Yang, D. Xia and Q. Xu, *Small*, 2015, **11**, 2511.

13 Y. Liu, X. Wang, X. Song, Y. Dong, L. Yang, L. Wang, D. Jia, Z. Zhao and J. Qiu, *Carbon*, 2016, **109**, 461.

14 F. Niu, J. Yang, N. Wang, D. Zhang, W. Fan, J. Yang and Y. Qian, *Adv. Funct. Mater.*, 2017, **27**, 1700522.

15 G. K. Zhao, C. Guo and C. M. Li, *J. Mater. Chem. A*, 2017, **5**, 19195.

16 F. Zhang, C. Xia, J. Zhu, B. Ahmed, H. Liang, D. B. Velusamy, U. Schwingenschlögl and H. N. Alshareef, *Adv. Energy Mater.*, 2016, **6**, 1601188.

17 Y. Fang, X. Y. Yu and X. W. Lou, *Adv. Mater.*, 2018, **30**, 1706668.

18 K. Krishnamoorthy, P. Pazhamalai, G. K. Veerasubramani and S. J. Kim, *Electrochim. Acta*, 2016, **190**, 305.

19 J. -H. Kim, J. H. Yun and D. K. Kim, *Adv. Energy Mater.*, 2018, **8**, 1703499.

20 K. Krishnamoorthy, G. K. Veerasubramani and S. J. Kim, *Mater. Sci. Semicond. Process.*, 2015, **40**, 781.

21 J. -H. Kim, Y. H. Jung, J. H. Yun, P. Ragupathy and D. K. Kim, *Small*, 2018, **14**, 1702605.

22 Z. Hu, Z. Zhu, F. Cheng, K. Zhang, J. Wang, C. Chen and J. Chen, *Energy Environ. Sci.*, 2015, **8**, 1309.

23 A. Douglas, R. Carter, L. Oakes, K. Share, A. P. Cohn and C. L. Pint, *ACS Nano*, 2015, **9**, 11156.

24 M. Walter, T. Zund and M. V. Kovalenko, *Nanoscale*, 2015, **7**, 9158.

25 F. Bu, P. Xiao, J. Chen, M. F. Aly Aboud, I. Shakir and Y. Xu, *J. Mater. Chem. A*, 2018, **6**, 6414.

26 Y. J. Fang, Z. X. Chen, L. F. Xiao, X. P. Ai, Y. L. Cao and H. X. Yang, *Small*, 2018, **14**, 1703116.

27 Y. X. Wang, J. Yang, S. L. Chou, H. K. Liu, W. X. Zhang, D. Zhao and S. X. Dou, *Nat. Commun.*, 2015, **6**, 8689.

28 W. Chen, S. Qi, L. Guan, C. Liu, S. Cui, C. Shen and L. Mi, *J. Mater. Chem. A*, 2017, **5**, 5332.

29 X. Wei, W. Li, J. a. Shi, L. Gu and Y. Yu, *ACS Appl. Mater. Interfaces*, 2015, **7**, 27804.

30 K. Zhang, M. Park, L. Zhou, G. H. Lee, J. Shin, Z. Hu, S. L. Chou, J. Chen and Y. M. Kang, *Angew. Chem., Int. Ed.*, 2016, **55**, 12822.

31 L. Li, S. Peng, N. Bucher, H. Y. Chen, N. Shen, A. Nagasubramanian, E. Eldho, S. Hartung, S. Ramakrishna and M. Srinivasan, *Nano Energy*, 2017, **37**, 81.

32 Y. Xiao, J. Y. Hwang, I. Belharouak and Y. K. Sun, *ACS Energy Lett.*, 2017, **2**, 364.

33 H. Geng, J. Yang, Z. Dai, Y. Zhang, Y. Zheng, H. Yu, H. Wang, Z. Luo, Y. Guo, Y. Zhang, H. Fan, X. Wu, J. Zheng, Y. Yang, Q. Yan and H. Gu, *Small*, 2017, **13**, 1603490.

34 S. Li, J. Niu, Y. C. Zhao, K. P. So, C. Wang, C. A. Wang and J. Li, *Nat. Commun.*, 2015, **6**, 7872.

35 Z. Liu, T. Lu, T. Song, X. Y. Yu, X. W. Lou and U. Paik, *Energy Environ. Sci.*, 2017, **10**, 1576.

36 L. Yang, S. Li, J. Liu, K. Zhu, S. Liu and M. Lei, *J. Mater. Chem. A*, 2017, **5**, 1629.

37 Z. S. Wu, W. Ren, L. Xu, F. Li and H. M. Cheng, *ACS Nano*, 2011, **5**, 5463.

38 X. Liu, J. Zhang, S. Guo and N. Pinvaluena, *J. Mater. Chem. A*, 2016, **4**, 1423.

39 B. Wu, H. Song, J. Zhou and X. Chen, *Chem. Commun.*, 2011, **47**, 8653.

40 J. Kong, C. Zhao, Y. Wei and X. Lu, *ACS Appl. Mater. Interfaces*, 2015, **7**, 24279.

41 Y. El Mendili, A. Abdelouas and J. F. Bardeau, *Phys. Chem. Chem. Phys.*, 2013, **15**, 9197.

42 G. K. Veerasubramani, K. Krishnamoorthy and S. J. Kim, *J. Power Sources*, 2016, **306**, 378.

43 C. Wang, M. Lan, Y. Zhang, H. Bian, M. F. Yuen, K. Ostrikov, J. Jiang, W. Zhang, Y. Y. Li and J. Lu, *Green Chem.*, 2016, **18**, 3029.

44 K. Zhang, T. Zhang, J. Liang, Y. Zhu, N. Lin and Y. Qian, *RSC Adv.*, 2015, **5**, 14828.

45 Y. He, P. Xu, B. Zhang, Y. Du, B. Song, X. Han and H. Peng, *ACS Appl. Mater. Interfaces*, 2017, **9**, 38401.

46 T. Brezesinski, J. Wang, S. H. Tolbert and B. Dunn, *Nat. Mater.*, 2010, **9**, 146.

47 J. Liu, J. Wang, C. Xu, H. Jiang, C. Li, L. Zhang, J. Lin and Z. X. Shen, *Adv. Sci.*, 2018, **5**, 1700322.

48 R. Elazari, G. Salitra, Y. Talyosef, J. Grinblat, C. S. Kelley, A. Xiao, J. Affinito and D. Aurbach, *J. Electrochem. Soc.*, 2010, **157**, A1131.

49 X. Xia, C. Zhu, J. Luo, Z. Zeng, C. Guan, C. F. Ng, H. Zhang and H. J. Fan, *Small*, 2014, **10**, 766.

50 R. Purbia and S. Paria, *Nanoscale*, 2015, **7**, 19789.

51 J. Lee, J. C. Park and H. Song, *Adv. Mater.*, 2008, **20**, 1523.

52 J. Lee, J. C. Park, J. U. Bang and H. Song, *Chem. Mater.*, 2008, **20**, 5839.

53 J. Liu, S. Z. Qiao, S. Budi Hartono and G. Q. Lu, *Angew. Chem., Int. Ed.*, 2010, **49**, 4981.

54 Z. Wei Seh, W. Li, J. J. Cha, G. Zheng, Y. Yang, M. T. McDowell, P. C. Hsu and Y. Cui, *Nat. Commun.*, 2013, **4**, 1331.